



PANI/FeUiO-66 nanohybrids with enhanced visible-light promoted photocatalytic activity for the selectively aerobic oxidation of aromatic alcohols

Xueqing Xu, Ruxue Liu, Yuhang Cui, Xixi Liang, Cheng Lei, Shuangyan Meng, Yali Ma, Ziqiang Lei, Zhiwang Yang *

Key Laboratory of Polymer Materials of Gansu Province Key Laboratory of Eco-Environment-Related Polymer Materials, Ministry of Education, College of Chemistry and Chemical Engineering, Northwest Normal University, Lanzhou, 730070, China

ARTICLE INFO

Article history:

Received 12 January 2017

Received in revised form 30 March 2017

Accepted 6 April 2017

Available online 7 April 2017

Keywords:

Photocatalysis

MOFs

PANI

FeUiO-66

Aerobic oxidation of alcohols

ABSTRACT

Metal-organic frameworks (MOFs), a new class of porous crystalline materials, have attracted great interest as fascinating applications for eco-friendly photocatalysts. In this study, new hybrid MOFs, iron doped zirconium based metal-organic frameworks, FeUiO-66, were successfully synthesized by hydrothermal method firstly. Then the PANI/FeUiO-66 nanohybrids were fabricated through annealing process. The photocatalytic performances of the obtained PANI/FeUiO-66 nanohybrids were evaluated by selectively oxidation of various alcohol substrates using molecular oxygen as a benign oxidant. Boosting by synergistically multi-doped effect, the catalytic activity of the novel PANI/FeUiO-66 is remarkably higher than that of bare UiO-66 under visible light irradiation at ambient temperature. Further analyses revealed that the enhancement of photocatalytic activity originated from the two aspects. On one hand, when the Fe doped into the framework, valence fluctuation of $\text{Fe}^{2+}/\text{Fe}^{3+}$ could reduce the recombination rate of photoexcited carriers. On the other hand, based on energy band matching between FeUiO-66 and PANI, the easily formed heterostructures from PANI and FeUiO-66 can efficiently enhance the separation of photogenerated carriers. Furthermore, by virtue of unique advantage of the position of the CB and VB of FeUiO-66, alcohols could be selectively oxidized by the $\cdot\text{O}_2^-$ and h^+ . Remarkably, it is expected that the MOF-conductive conjugated polymers nanohybrids could be used as efficient visible light driven photocatalysts for organic transformation with high selectivity under eco-friendly conditions.

© 2017 Elsevier B.V. All rights reserved.

1. Introduction

One of the challenges in chemistry field is the development of renewable and green energy based processes. Photocatalytic conversion of organic compounds by utilizing light energy is the candidate for a variety of environmentally benign organic transformations [1]. Moreover, heterogeneous photocatalysis also can provide a new synthetic method since it requires milder conditions and allows shorter reaction sequences minimizing side processes [2]. Therefore, there is a great interest in designing materials with efficient visible light photocatalysts for driving important chemical processes. A case in point, the selective oxidation of alcohols to aldehydes or ketones is one of the fundamental chemical conversions in industrial applications and organic synthesis. Additionally, from both economic and environmental point of view,

photocatalytic oxidation of alcohols with O_2 as an inexpensive primary oxidant has the potential research value [3–5]. Up to now, researchers have realized the selective oxidation of aromatic alcohols using O_2 as the oxidant over modified TiO_2 , CdS , Bi_2WO_6 , $\text{g-C}_3\text{N}_4$ and WO_3 etc. under visible light irradiation [4,6–8]. These works prominently enhanced on the improvement of the photocatalytic activity and selectivity for the aerobic oxidation of alcohols. However, to develop more efficient and eco-friendly photocatalysts with new structures were still a great challenge.

As a consequence, emerging as a new class of highly porous crystalline materials with fine-tunable and uniform pore structures, metal-organic frameworks (MOFs) are constructed by joining the inorganic secondary building units (metal ions or clusters) with organic linkers [9–11]. Expect for the huge progress in expanding new MOFs families, it is attracted extensive attention for exploiting their applications including gas storage, separation, molecular sensing and catalysis et al. [12–14]. According to previous study, it is demonstrated that the metal clusters in MOFs can be regarded as inorganic semiconductor quantum entities while the organic

* Corresponding author.

E-mail address: yangzw@nwnu.edu.cn (Z. Yang).

linkers as antenna which activate these semiconductor quantum dots via the linker to metal cluster charge-transfer (LMCT) upon light excitation [15,16]. Up to date, more and more photocatalysts based on MOFs have been applied in CO₂ reduction, degradation of pollutant substance, hydrogen evolution, and organic syntheses [16–18].

From the previous studies, it is generally accepted that the strategy for improving the utilization efficiency of photogenerated electron-hole pairs and prolonging the lifetime of photogenerated charge-carriers could enhance the photocatalytic activity of MOFs [19]. On one hand, the compositions, structures and properties of MOFs are easily adjusted by varying the metal ions and organic ligands [20,21]. Herein, metal doping has already been demonstrated to be an effective method for enhancing the performance of MOFs. Incorporation of metal-to-metal charge transfer (MMCT) by metal substitution to construct bimetallic assemblies in semiconductors can enhance their photocatalytic performance [22]. Recently, Yamashita et al. synthesized a new photoactive cerium-doped chromium based amine-functionalized MOF(CeMIL-101) for the hydrolysis of ammonia borane under visible light irradiation [23]. Zhu and his colleagues reported that the selective photocatalytic oxidation of alcohols to their corresponding aldehydes using O₂ as oxidant can be achieved over Ni-doped NH₂-MIL-125(Ti) upon visible light irradiation [15]. Moreover, it is also demonstrated by the Li's group that doped metal cations can also act as electron mediators to facilitate charge transfer processes [24]. To achieve this overall modular design, the composite should contain redox-active (multi) metallic nodes such as Fe, Co, Cu, and Ni etc. to allow charge separation and accumulation of electrons [15]. Therefore, in the current work, Fe-doped UiO-66 catalyst (FeUiO-66) has been prepared firstly to improve the photocatalytic activity of the UiO-66.

On the other hand, more and more concerns have focused on multi-component heterojuncted photocatalysts which can also promote the charge separation from one component to another, thereby increase the photocatalytic activity [25]. Delocalized π - π conjugated structures have been proven to induce a rapid photoinduced charge separation rate in electron-transfer processes. Recently, many research teams have developed some hybrid semiconductors with delocalized conjugative structure materials as efficient photocatalysts, such as graphene (GR), carbon nitride (C₃N₄), and conductive polyaniline (PANI) [26–28]. Among these π - π conjugated structures, PANI has received increasing attention due to its advantages of low cost, easy synthesis, high conductivity and excellent environmental stability. Most importantly, the combination of PANI with semiconductor could improve the migration efficiency of photocarriers at the interface between PANI and semiconductor, thereby it could facilitate the separation of photo-generated carriers and enhancing the photocatalytic performance.

Taking all of these into consideration, to improve the photocatalytic activities of MOFs, herein we present a simple, eco-friendly method to prepare a novel hybrid photocatalyst PANI/FeUiO-66. The new hybrid structure was used as photocatalysts for the aerobic oxidation of aromatic alcohols to the corresponding aldehydes with O₂ as oxidant under visible light irradiation. The results also showed that the PANI/FeUiO-66 could effectively improve the photoactivity of the oxidation of aromatic alcohols.

2. Experimental

2.1. Materials

All reagents are analytical purity. Aniline monomer (AN, Tianjin Chemical Reagent Co., Tianjin, China) was distilled under reduced pressure. Ammonium persulfate (APS) was purchased

from Tianjin Guangfu Fine Chemical Industry Research Institute. 1,4-Benzenedicarboxylic acid (H₂BDC), zirconium tetrachloride (ZrCl₄), benzyl alcohol, 4-methoxybenzyl alcohol were obtained from Aladdin Reagent Co., Ltd. *N*, *N*-dimethylformamide (DMF), citric acid (CA), iron chloride hexahydrate (FeCl₃·6H₂O) were purchased from Shanghai Chemical Reagent Co.; 4-Nitrobenzyl alcohol, 2-methylbenzyl alcohol, 4-chlorobenzyl alcohol, 2-methoxybenzyl alcohol, 4-hydroxybenzyl alcohol, benzhydrol, 4-chlorobenzhydrol, and 4-methoxybenzhydrol were obtained from Beijing J&K Scientific Co. Ltd. 4-Methylbenzyl alcohol, 4, 4'-dimethylbenzhydrol, 4, 4'-dimethoxylbenzhydrol and 4, 4'-dichlorobenzhydrol were obtained from Alfa Aesar Co. Ltd.

2.2. Preparation of photocatalysts

2.2.1. Synthesis of FeUiO-66

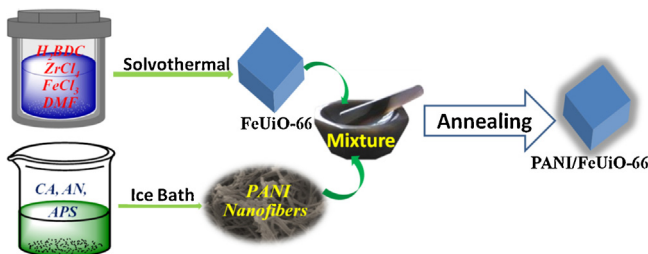
A series of FeUiO-66 nanocomposites with different mole ratios of FeCl₃·6H₂O vs ZrCl₄ were synthesized by a facile one-pot solvothermal reaction. In a typical synthesis, ZrCl₄ (1 mmol) and H₂BDC (1 mmol) were first dissolved in 60 mL of DMF. A series of variational amount of FeCl₃·6H₂O were then added into the above solution and continuous stirring for 1 h, respectively. The clear and yellow solution was then transferred into a 100 mL Teflon-lined stainless steel autoclave and heated to 120 °C for 48 h. After cooled to room temperature, the products were collected by centrifugation and washed with DMF and anhydrous ethanol three times, respectively, and then the solid was dried at 110 °C under vacuum for 12 h to remove the excess of unreacted organic linkers and DMF. As a contrast, the UiO-66 was also prepared according the same methods; the only difference is the absence of FeCl₃·6H₂O. The obtained products were named as FeUiO(*x*) (*x* = 1:1; 1:2; 1:5 and 1:10, which stand for the mole ratios of FeCl₃·6H₂O vs ZrCl₄).

2.2.2. Synthesis of PANI nanostructure

The PANI nanostructure was synthesis according to the literature report [29]. A typical experimental process for the preparation of PANI nanostructure was as follows. 0.263 g of CA as a template was added into 80 mL of distilled water and stirred for 0.5 h at room temperature. Then 0.5 mL of AN was added into the above solution and stirred for 30 min. Subsequently, 20 mL of aqueous solution containing 1.14 g of APS was added drop by drop into the reaction mixture and the resultant solution was allowed to stand for 12 h in an ice bath. The resulting precipitate was washed several times with deionized water and ethanol, respectively. Finally, the product was dried in a vacuum oven at 60 °C for 24 h to obtain a dark green powder.

2.2.3. Synthesis of PANI/FeUiO-66 nanohybrids

The PANI/FeUiO-66 nanohybrids were fabricated by thermal treating of the mixture of PANI and FeUiO-66 octahedrons. In a typical procedure, 0.2 g of FeUiO-66 octahedrons and 2 mg of PANI powder was mixed with 1 mL of ethanol in the mortar and the mixture was ground until the ethanol was evaporated completely. In order to keep the structure of the FeUiO-66 and PANI, an appreciate temperature is necessary. According to the thermogravimetric analyses (TGA) results for the UiO-66, FeUiO-66 and PANI, the ground mixture was then thermal treated at 300 °C for 4 h in N₂ atmosphere in a tube furnace. Moreover, in the heating progress the PANI could be dispersed on the surface of FeUiO-66, then the PANI gathered in the surface of FeUiO-66, it is easy to make PANI be coated on FeUiO-66 and form the heterojunction. According to the atomic absorption spectroscopy analysis, the actual content of Fe element in FeUiO(1:5) and PANI/FeUiO(1:5) are 0.40% and 0.72%, respectively. It also could find that some impurities could be removed in the annealing process, so that Fe element in the



Scheme 1. The illustration for the preparation of PANI/FeUiO-66 nanohybrids.

PANI/FeUiO(1:5) have a slightly increase. Whole of the experimental process was also presented in the **Scheme 1**.

2.3. Catalyst characterization

Power X-ray diffraction (XRD) data were gathered on a Rigaku D/Max-2400 with Cu $\text{K}\alpha$ radiation at 40 kV and 40 mA. Fourier transform infrared (FT-IR) spectroscopy with KBr pellets was conducted on a Nicolet NEXUS 670 spectrometer in the scanning range of 4000–400 cm^{-1} . UV-vis diffuse reflectance spectra (UV-vis DRS) of the catalysts were characterized by a Cary 500 UV-vis-NIR spectrophotometer, using BaSO_4 as the internal reflectance standard. The photoluminescence (PL) spectrum for samples were conducted on a PELS-55 luminescence/fluorescence spectrophotometer. The morphology of the samples was characterized by field emission scanning electron microscopy (FE-SEM, Ultra Plus, Carl Zeiss, Germany) and transmission electron microscopy (TEM, a JEOL model JEM2010 EX microscope at an accelerating voltage of 200 kV). An X-ray photoelectron spectroscopy (XPS, ThermoVG Scientific Sigma Probe using an Al $\text{K}\alpha$ radiation) method was used to study the surface compositions of the catalysts. The thermogravimetric analysis (TGA) was performed from room temperature to 800 $^{\circ}\text{C}$ at the ramping of 5 $^{\circ}\text{C min}^{-1}$ in N_2 atmosphere on a TA Instruments Discovery Thermogravimetric Analyzer. The specific surface areas and pore size distributions were calculated by using N_2 adsorption-desorption isotherms and Brunauer-Emmett-Teller (BET) method. The atomic absorption spectroscopy (Varian companies in the United States, AA240) was used to analyze the content of Fe element in the catalysts.

2.4. Photocatalytic experimental details

Photocatalytic reactions were carried out using a 500 W xenon lamp (BiLon Co. Ltd., with a 400 nm cutoff filter, $\lambda > 400$ nm) equipped with a cold water circulation device. For the photocatalytic oxidation of alcohols, 5 mg of the catalyst mixed with 0.2 mmol of alcohol was added into 6 mL of solvent in a quartz vial.

3. Results and discussion

3.1. Characterization

XRD was used to characterize the composition and crystal form of different samples. **Fig. 1** shows the XRD patterns of UiO-66, FeUiO-66 series, PANI and PANI/FeUiO-66 series composites. For the diffraction pattern of UiO-66 and FeUiO-66 (**Fig. 1a**), it is observed that pristine UiO-66 fits well with that given in the previous reports and fitting data, providing clear evidence of the

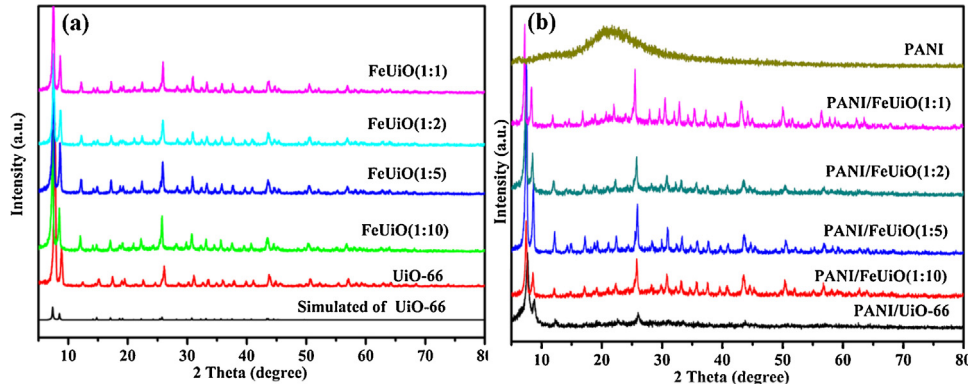


Fig. 1. XRD patterns of samples.

4. Conclusion

UiO-66 and FeUiO-66 series, PANI and PANI/FeUiO-66 series composites. For the diffraction pattern of UiO-66 and FeUiO-66 (**Fig. 1a**), it is observed that pristine UiO-66 fits well with that given in the previous reports and fitting data, providing clear evidence of the

Before visible light illumination, the above suspension was stirred in the dark for 1 h to ensure the establishment of an adsorption-desorption equilibrium between the catalyst and reactant. After the reaction, the solution was collected at a certain time interval and centrifuged to remove the catalyst completely at 8000 rpm. The conversion and the selectivity of alcohols were recorded through gas chromatograph (GC) analyses on a Shimadzu GC-2010 equipped with a RTX-1 capillary column and a FID detector. The whole experimental process was conducted under O_2 atmosphere. The conversion and the selectivity in the reaction process could be calculated by the Formulas (1) and (2), respectively.

$$\text{Conversion of the alcohol (\%)} = \frac{C_0 - C_n}{C_0} \times 100\% \quad (1)$$

$$\text{Selectivity of the aldehyde/ketone (\%)} = \frac{C_a}{C_0 - C_n} \times 100\% \quad (2)$$

Where C_0 is the initial concentration of alcohol prior to reaction, C_n and C_a is the concentration of alcohol and aldehyde/ketone measured at the time t , respectively.

2.5. Electrochemical measurements

The Mott-Schottky plot and the electrochemical impedance spectroscopy (EIS) were measured on an electrochemical analyzer (Aotolab, America). EIS tests were carried out with AC impedance-potential model in a standard three-electrode system. Namely, a Ag/AgCl electrode, a Pt foil electrode and a FTO glass electrodes served as the reference electrode, counter electrode and working electrodes, respectively. The progress was performed under dark condition at open circuit potential over the frequency range between 10^5 and 10^{-2} Hz, with an AC voltage magnitude of 5 mV in 0.2 M Na_2SO_4 solution. For the preparation of photocatalyst-based composite electrodes, the prepared photocatalysts were dispersed in chitosan solution to form 5 mg mL^{-1} solution and ultrasonicated for 30 min, after then 0.1 mL of colloidal solution was dropped on the conductive side of the FTO glass and allowed to dry at room temperature and then 100 $^{\circ}\text{C}$ in the air for 24 h.

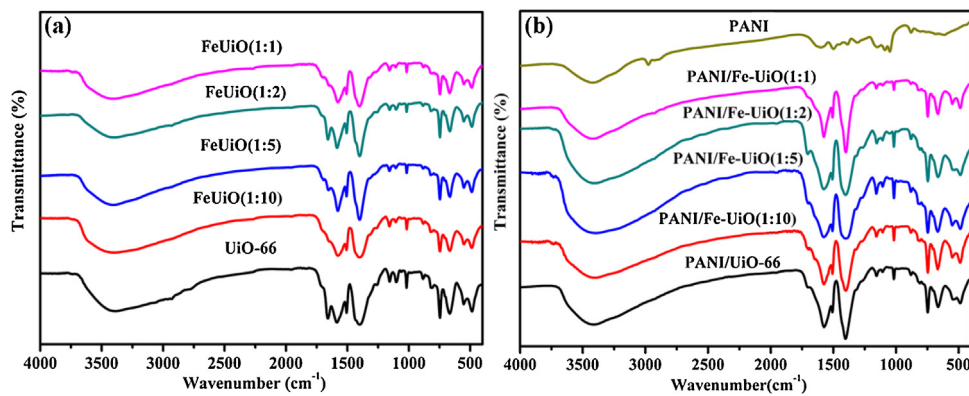


Fig. 2. FT-IR spectra of the samples.

successful synthesis of UiO-66 [30]. FeUiO-66 maintained the similar characteristic peaks as that of UiO-66, and no characteristic peak of Fe is found due to the low loading and high dispersion of Fe^{3+} on the surface of UiO-66, suggesting the crystalline structure of UiO-66 was well preserved after the loading of the Fe^{3+} . It indicates that incorporation of Fe^{3+} does not alter the crystal growth of the UiO-66 units. As can be seen from Fig. 1b, for the PANI, the two broad diffraction peaks at 19° and 25° are attributed to the periodicity parallel to the polymer chains of PANI [31]. For the PANI/FeUiO-66 nanohybrids, the XRD pattern of it is similar to that of the bare FeUiO-66 and UiO-66, respectively. It is proved that the structure of UiO-66 and FeUiO-66 has been well maintained. Besides, it is worth noting that no typical diffraction peaks of PANI appear in the PANI/FeUiO-66 nanohybrids, which is attributed to the low weight loading of PANI on the surface of the FeUiO-66 nanocomposites [26]. The FT-IR spectra of PANI, UiO-66 and PANI/FeUiO-66 nanohybrids were also performed to illustrate the structure of the photocatalysts. As showed in Fig. 2a, for UiO-66, the broad peak located at 3420 cm^{-1} is assigned to the O–H vibration, indicating the presence of bound water and free water in the UiO-66 samples. The weak band detected at 1660 cm^{-1} was assigned to the stretching vibrations of $\text{C}=\text{O}$ in the carboxylic acid present in H_2BDC . The peaks observed at 1573 cm^{-1} and 1393 cm^{-1} were being identified as the asymmetric and symmetric vibrations of carboxyl groups, respectively. Moreover, the value of $\Delta\nu$ ($\Delta\nu = \nu_{\text{as}}(\text{COO}) - \nu_{\text{s}}(\text{COO})$) is 180 cm^{-1} , which is agree with the characteristic bridge coordination mode of that for UiO-66 [32]. In addition, the peak found at 1113 cm^{-1} is related to the C–O stretching vibration. The peaks at 821 , 745 and 667 cm^{-1} were due to the O–H and C–H vibration in the H_2BDC ligand. Compared with the bare UiO-66, the spectra of the FeUiO-66 composites did not change much, indicating that the structure of the UiO-66 is not destroyed after the Fe^{3+} doped into the UiO-66. In Fig. 2b, the main characteristic peaks of pure PANI can be assigned as follow: the band at 3400 cm^{-1} is regarded as the amine and imine sites, the signals at 1600 and 1498 cm^{-1} can be assigned to the quinonoid and benzenoid rings, respectively. The bands at 1307 and 1240 cm^{-1} are ascribed to the C–N and C=N stretching band of aromatic amine, while the band at 1150 cm^{-1} is assigned to the quinonoid unit of PANI, and the peak at 803 cm^{-1} is for the C–H bond in the benzenoid unit [33,34]. For the PANI/FeUiO-66 nanohybrids, the intensity of peaks for pure PANI at 1600 cm^{-1} and 1307 cm^{-1} become weaker, indicating the chemical bonds were weakened in PANI/FeUiO-66 nanohybrids. So that the PANI conjugated bond was stretched and a more conjugated structure containing PANI and FeUiO-66 formed.

The SEM and TEM images of the samples have been shown in Fig. 3. For the PANI, it exhibits chaotic three dimensional nanofibers status (Fig. 3a). UiO-66 presents an agglomerated cubical shape (Fig. 3b). Interestingly, the FeUiO-66 series have showed the differ-

ent morphology comparing with that of UiO-66. For FeUiO(1:10), they presents an agglomerated but regular cubical shape. For the other FeUiO-66 series, the dispersed and regular cubic with the size of about 80 nm could be observed (Fig. 3c–f). This morphologic evolution clearly indicated that the doped content of Fe^{3+} has an effect to the size of the FeUiO-66. The SEM image of obtained PANI/FeUiO(1:5) was displayed in Fig. 3g. Apparently, it is observed that the surface of PANI/FeUiO(1:5) becomes smoother owing to the PANI shell coated on the surface of FeUiO(1:5). Typical TEM images of the PANI/FeUiO(1:5) nanohybrid with different magnification have been shown in Fig. 3h and i. It can be clearly observed that the PANI nanosheets are intimately adhering on the edges of FeUiO(1:5) octahedrons. Most importantly, the clear interface between FeUiO(1:5) and PANI was formed during the coating process. It is important for efficient charge transfer between FeUiO-66 and PANI, thereby expects to improve the photocatalytic activity.

Further analysis of the XPS data provides information about the chemical composition and valence state in the PANI/FeUiO(1:5). XPS survey scan indicated the presence of O, N, C and Zr elements in the sample (Fig. 4a). However, the peak of Fe is not appeared in the survey scan on account of the little content of it. Besides, the atom content of the Fe, O, N, C and Zr on the surface of PANI/FeUiO(1:5) is 0.53% , 28.66% , 0.53% , 66.79% , and 3.84% , respectively. In the high-resolution C 1s XPS spectra (Fig. 4b), the fitted peaks at 288.6 eV , 286.3 eV and 284.5 eV can be attributed to the carboxylate carbon $\text{O}=\text{C}=\text{O}$, carbonyl carbon ($\text{C}=\text{O}$) and $\text{C}=\text{C}$ bond, respectively [29,35]. These above fitted peaks refer to the H_2BDC in the framework of FeUiO(1:5). While the peaks at 285.6 eV , 285.0 eV and 284.0 eV can be assigned to the C–N, C–H and C–C bond, respectively, which indicated the existence of PANI. The N 1s spectra (Fig. 4c) can be fitted into three components. The peak at 401.7 eV is assigned to the C–N bond, peak at 400.7 eV can be attributed the nitrogen cation ($\text{N}=\text{H}^+$) and the peak at 398.9 eV can be assigned to the imine-like nitrogen ($\text{C}=\text{N}=\text{C}$) in PANI [36]. The binding energy of O element (Fig. 4d) can be deconvoluted into three peaks at 530.6 , 531.5 and 532.6 eV , respectively. The primary peak at 530.6 eV is attributed to the Zr–O and Fe–O bond on the FeUiO-66, the second one at 531.5 eV is attributed to $\text{C}=\text{O}$ in H_2BDC , the last one is assigned to the hydroxyl groups [37,38]. For Zr (Fig. 4e), the curves of Zr 3d region can be deconvoluted into four peaks which are belong to the $\text{Zr 3d}_{5/2}(182.1\text{ eV}$ and 183.1 eV) and $\text{Zr 3d}_{3/2}(185.5\text{ eV}$ and 184.3 eV) respectively, which indicated the existence of Zr^{4+} [35]. The Fe 2p core level spectrum (Fig. 4f) consists of $\text{Fe 2p}_{3/2}$ and $\text{Fe 2p}_{1/2}$ excitations. The Fe 2p core level could be deconvoluted into four peaks. The peaks at 709.2 eV for $\text{Fe 2p}_{3/2}$ and 723.6 eV for $\text{Fe 2p}_{1/2}$ are assigned to the existence of the Fe^{2+} , while the peaks at 710.9 eV for $\text{Fe 2p}_{3/2}$ and 727.6 eV for $\text{Fe 2p}_{1/2}$ are attributed to the Fe^{3+} . The peak appeared at 714.9 eV observed in the high resolution XPS confirm the existence of Fe–O species [39–42]. Besides, according

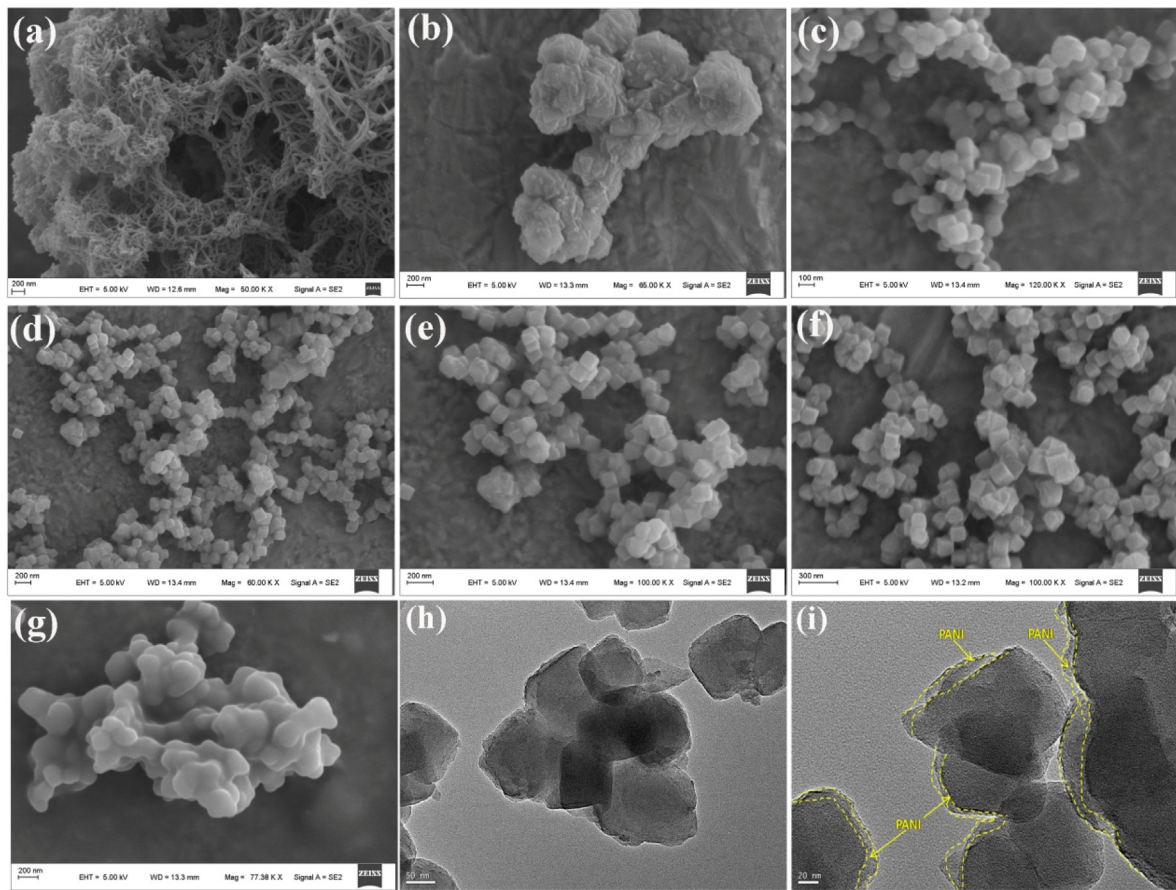


Fig. 3. FE-SEM images of PANI nanofibers (a); UiO-66 (b); FeUiO-66 series (1:10, 1:5, 1:2, 1:1 presented in c-f, respectively); PANI/FeUiO(1:5) (g) and TEM images of PANI/FeUiO(1:5) with different magnification (h and i).

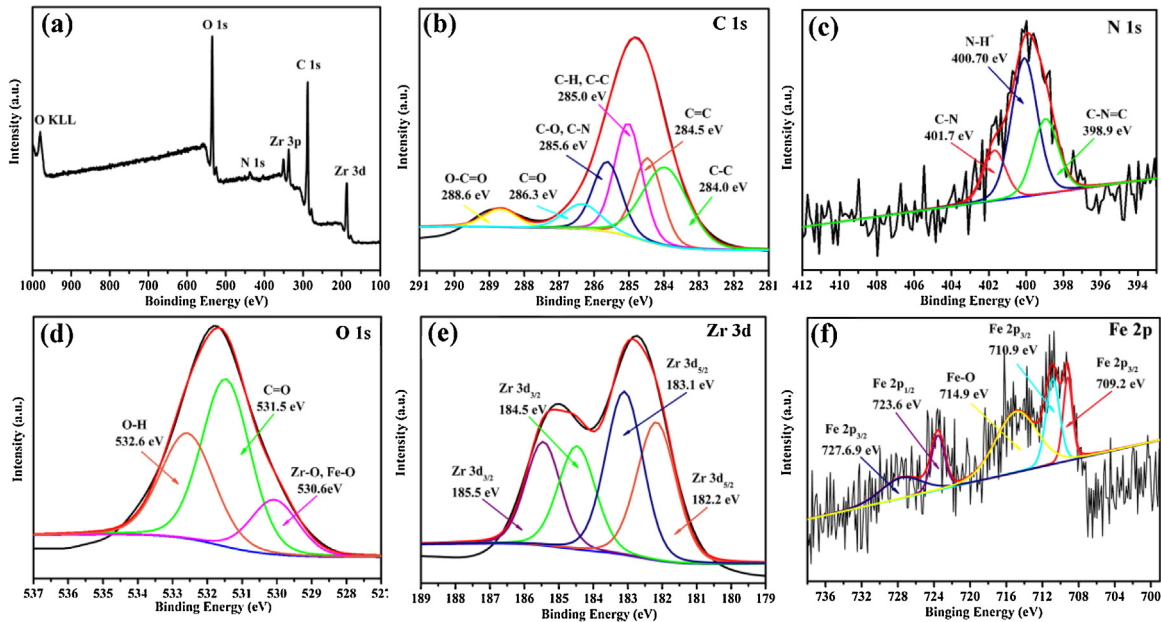


Fig. 4. XPS spectra of PANI/FeUiO(1:5): survey (a); C 1s (b); N 1s (c); O 1s (d); Zr 3d (e); Fe 2p (f).

to the analysis results of XRD, when the Fe doped into the UiO-66, the structure of the UiO-66 have not been changed. Moreover, it has not been observed the new diffraction peak about the ferric oxide species, so it could be confirmed that there have not presented the

ferric oxide species. The Fe has been doped into skeleton of the UiO-66. These results are further confirmed that the PANI/FeUiO-66 nanocomposites were prepared successfully.

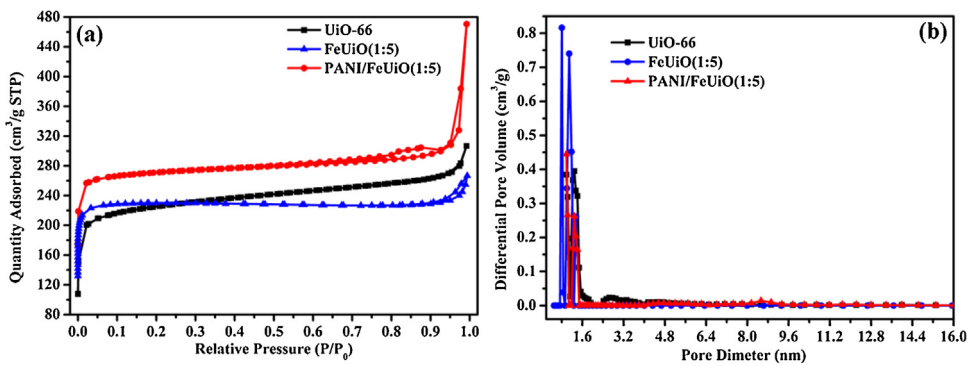


Fig. 5. Nitrogen adsorption-desorption isotherms (a) and pore size distribution curves (b) of the samples.

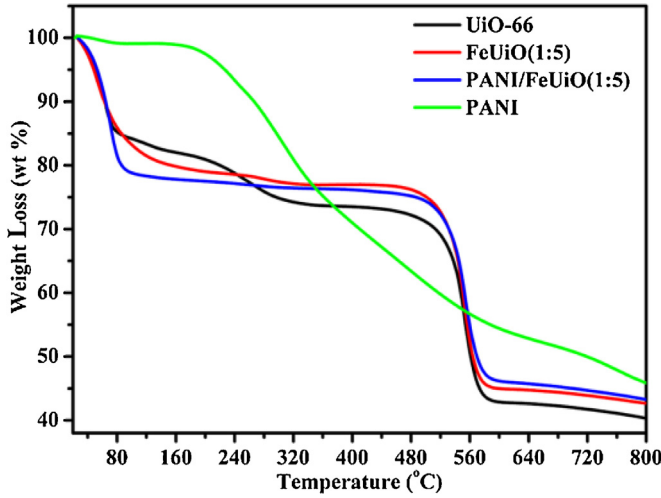


Fig. 6. TGA profiles of the samples.

The BET specific surface areas (S_{BET}) and pore sizes of the synthesized samples were analyzed by N_2 adsorption-desorption. As shown in Fig. 5a, the isotherm of UIO-66 belongs to the typical type I curve, indicating its typical microporous structure [35]. The BET specific surface area of UIO-66 is $866.5 \text{ m}^2 \text{ g}^{-1}$, and the average pore diameter is 1.2 nm. The BET surface area of FeUiO(1:5) is found to be $683.5 \text{ m}^2 \text{ g}^{-1}$, which is lower than the surface area of UIO-66. The average pore diameter of FeUiO(1:5) is 2.41 nm, suggesting that abundant micropore is existed in FeUiO(1:5). The average pore diameter of FeUiO(1:5) is higher than the average pore diameter of UIO-66. Therefore, it has great influence of pore structure and surface area for UIO-66 when Fe doped into the skeleton of UIO-66. The PANI/FeUiO(1:5) nanohybrid have higher specific surface areas than UIO-66 and the surface area is $1096.8 \text{ m}^2 \text{ g}^{-1}$, the average pore diameter is still 1.2 nm. Large specific surface areas of UIO-66, FeUiO(1:5) and PANI/FeUiO-66 are favorable for improving the photocatalytic activity.

Fig. 6 shows the results of thermogravimetric analyses (TGA) of PANI, FeUiO(1:5) and their composites in N_2 atmosphere. Weight loss profiles from TGA tests show that the as-synthesized UIO-66 presents three stages in weight loss. They can be attributed to surface water evaporation (below 120 °C), DMF decomposition (150–300 °C) and the structure collapse of UIO-66 (480–560 °C), respectively. Meanwhile FeUiO-66 presents higher thermal stability with little DMF decomposition, suggesting it maintains a strong thermal stability. UIO-66 and FeUiO-66 could also keep the structure up to 560 °C and after that it will decompose to form ZrO_2 [43]. TGA provided better understanding of the thermal stability of FeUiO-66. For the PANI, an initial mass loss around

100 °C was ascribed to the evaporation of surface absorbed water molecules. The second stage observed within the temperature range of 100–300 °C is related to the removal of dopant molecules from the polymer structure. The weight loss observed between 300 and 800 °C corresponds to the degradation of the polymer chain [29]. The PANI/FeUiO-66 compounds also have the similar weight loss trend as FeUiO-66. Above all, it is demonstrated that the prepared PANI/FeUiO-66 nanohybrids well maintained the structures of FeUiO-66 and PANI, respectively.

UV-vis DRS are widely used to measure the optical properties of the semiconductor powder materials. Fig. 7a shows the spectra of UIO-66, FeUiO-66, and PANI/FeUiO-66 nanohybrids. Both the absorptions occurred in the wavelength range of 200–400 nm. The spectrum of UIO-66 characterized by an absorption edge around 310 nm is ascribed to $\pi-\pi^*$ electronic jumping of the aromatic ring. Compared with UIO-66, the absorption edges of FeUiO-66 series were gradually red shifted with the increasing amount of the Fe^{3+} , indicating that the incorporation of the Fe^{3+} could improve the absorption of the UIO-66. For the PANI/FeUiO-66 series, the absorption edges of them were further red shifted. The enhanced absorbance of visible light is expected to improve the photocatalytic performance of PANI/FeUiO-66 toward the target reactions. Correspondingly, the band gap energy of a semiconductor could be calculated by the Kubelka-Munke equation, as shown in Fig. 7b, the transition bandgaps estimated from the onset of the curve edges were about 3.36, 3.23, 3.10, 3.09, 3.05, 3.0, 2.89, 2.76, 2.58, and 2.49 eV for UIO-66, FeUiO(1:10), FeUiO(1:5), FeUiO(1:2), FeUiO(1:1), PANI/UiO-66, PANI/FeUiO(1:10), PANI/FeUiO(1:5), PANI/FeUiO(1:2) and PANI/FeUiO(1:1), respectively. The relatively narrow band-gap energy observed for PANI/FeUiO-66 nanocomposites are likely attributed to the strong interaction of the hybrid structure, which enables more efficient utilization of the solar spectrum. The PL spectroscopy measurements were used to analyze the charge recombination of semiconductor. Fig. 7c presents the PL spectra of as-prepared photocatalysts. The pure UIO-66 exhibits a strong emission peak at around 378 nm. For the Fe doped sample of FeUiO-66, the PL emission intensity was lower than that of UIO-66. Moreover, the different amounts of Fe has the different emission intensity, FeUiO(1:5) has the lowest intensity, indicating that it could efficiently promote the separation photocarriers, when Fe doped into the framework of the UIO-66. When PANI was added, the PL emission intensity decreased markedly, which suggests that the photoinduced charge could be further separated with the heterojunction formed between FeUiO-66 and PANI. As shown in Fig. 7d, EIS Nyquist plots of the electrodes, which were made by the samples of UIO-66, FeUiO-66 and the PANI/FeUiO-66 nanohybrids, respectively, showing that PANI/FeUiO-66 has a much smaller arc than that of UIO-66 and FeUiO-66, suggesting the more efficient transfer of charge carriers over the surface of PANI/FeUiO-66. The order of PL intensity and the EIS are both agree

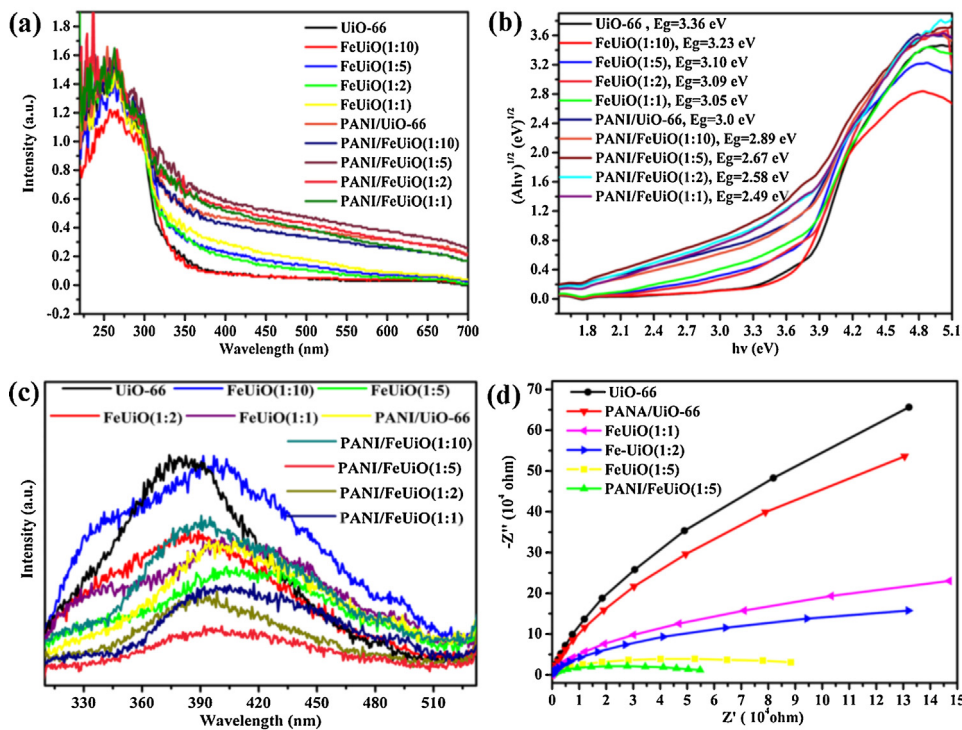


Fig. 7. UV/vis reflectance spectra (a); Relationship of $(Ahv)^{1/2}$ vs. $h\nu$ (b); PL spectra of samples (c); EIS Nyquist plots of samples (d).

Table 1

Blank control experiments of the photocatalytic oxidation by PANI/FeUiO-66 nanohybrids.

^a Entry	Catal.	^b Con.%	^c Sel.%
1	none	0	0
2	UiO-66	10	93
3	FeUiO-66(1:10)	13	96
4	FeUiO-66(1:5)	32	98
5	FeUiO-66(1:2)	25	98
6	FeUiO-66(1:1)	17	98
7	PANI/UiO-66	28	98
8	PANI/FeUiO(1:10)	45	98
9	PANI/FeUiO(1:5)	59	99
10	PANI/FeUiO(1:2)	47	99
11	PANI/FeUiO(1:1)	42	99
12 ^d	PANI/FeUiO(1:5)	3	99

a: Conditions: catalyst (5 mg); benzyl alcohol (0.2 mmol); light (>400 nm); reaction time (5 h); b and c: Calculated by GC analysis; d: Without the visible light.

well with the observed results of their photocatalytic activity mentioned below. Therefore, the formation of a conjugated structure between the PANI and FeUiO-66 over a wide range facilitates the migration efficiency of photo-induced charges and suppresses the charge recombination, thus enhancing the photocatalytic performance of PANI/FeUiO-66.

3.2. Photocatalytic activity for the oxidation of alcohols

The photocatalytic efficiency of PANI/FeUiO-66 was evaluated by the selective oxidation of benzyl alcohol (BA) to benzaldehyde (BAD). The reaction was conducted using O_2 as the oxidant under visible light irradiation. The corresponding results were summarized in Table 1. Comparing with UiO-66, significant improvement for the catalytic activity was achieved by FeUiO-66 and PANI/FeUiO-66. The conversion of BA is only 10% when used UiO-66 as the catalyst, it could be due to its limited absorption of visible light. When the Fe doped, the conversion by FeUiO(1:5) and PANI/FeUiO(1:5) were enhanced to 32 and 59% at the same con-

Table 2

Photooxidation of benzyl alcohol in different solvents.

^a Entry	Sol.	^b Con.%	^c Sel.%
1	acetonitrile	53	99
2	toluene	36	99
3	ethyl acetate	60	99
4	cyclohexane	11	99
5	acetone	30	99
6	1, 4-dioxane	10	99
7	1, 2-dichloroethane	59	99
8	DMF	35	99

a: Conditions: PANI/FeUiO(1:5) (5 mg); benzyl alcohol (0.2 mmol); light (>400 nm); reaction time (5 h); b and c: Calculated by GC analysis.

ditions, respectively (Table 1 entries 2, 4 and 9). The controlled experiments were also conducted in the absence of visible light (entry 12) or without catalysts but under visible light irradiation (entry 1) for 5 h. It is shown that BA is hardly oxidized in the absence of visible light or without catalyst but under visible light irradiation. Therefore, the oxidation of BA to BAD is a photodriven reaction. Beside, for the series of FeUiO-66, they have the different effectiveness for the oxidation reaction owing to the size and their absorption for the visible light (entries 3–6). Among the FeUiO-66 series, FeUiO(1:5) has obtained the best conversion of the BA (32%) under the same conditions. A similar conclusion also could be adapted for the series of PANI/FeUiO-66 (entries 7–11). Moreover, the PANI/FeUiO(1:5) has the highest conversion (59%).

As shown in Table 2, different solvents such as toluene, acetonitrile, ethyl acetate, cyclohexane, acetone, 1, 2-dichloroethane and 1, 4-dioxane and DMF have different influence on the oxidation reactions. Ethyl acetate is an ideal solvent for this aerobic selective oxidation. After the screening of the solvents, the substrate scope of the aromatic alcohols photocatalytic aerobic oxidation over PANI/FeUiO-66 was also investigated and the results are summarized in Table 3. Remarkably, the selected aromatic alcohols are converted into the corresponding aldehydes or ketones with high selectivity and conversion in all the cases. In addition, it appears

Table 3

Photooxidation of various substituted benzyl alcohols over PANI/FeUiO(1:5).

^a Entry	Sub.	Pro.	^b Con.%	^c Sel.%
1			61	99
2			82	98
3			77	98
4			39	98
5			49	98
6			20	98
7			10	94
8			100	100
9			38	100
10			22	100
11			90	100
12			98	100

a: Conditions: PANI/FeUiO(1:5) (5 mg); substrate (0.2 mmol); light (>400 nm); reaction time (5 h); b and c: Calculated by GC analysis.

that the electronegativity of the substituent has a significant impact on the conversions over PANI/FeUiO-66. In comparison with benzyl alcohol, the alcohols those bearing an electron donating substituent on the *o*-position of phenyl ring exhibit the enhanced conversions (**Table 3, entries 1–3**) while those bearing an electron donating substituents on the *p*-position of phenyl ring or an electron withdrawing ones show the decreased conversions (**entries 4 and 7**). Moreover, for the benzhydrol, the highest conversion is obtained, it could be attribute that the diphenyl ketone has the highest stability(**entries 8**), however the conversion for other derivatives of benzhydrol were decreased with different extent, it could be related with the Space steric hindrance for the different substituent group(**entries 9–12**).

3.3. Reusability of the photocatalyst

The reusability of the photocatalyst is also very important for the catalysts to be applied practically. Herein the photocatalytic cycling tests for BA oxidation were performed to investigate the reusability of PANI/FeUiO-66. **Fig. 8a** shows that after four cycles of photocatalytic oxidation of BA, the BAD conversion over PANI/FeUiO(1:5) only exhibits a slight decrease of 5%, therefore, PANI/FeUiO-66 performed good reusability in the oxidation. To assess the structural

stability, we examined the crystalline structures of as-prepared and the six-time-reused PANI/FeUiO(1:5) nanohybrid by FT-IR and XRD. As shown in **Fig. 8b**, no extra characteristic diffraction peaks were observed in XRD spectra pattern of PANI/FeUiO(1:5), which implied that the position and the intensity of the peaks are nearly the same and no new peaks occurred and no evident crystalline structure changes after the photocatalytic reaction. The FT-IR spectra of the PANI/FeUiO(1:5) sample was shown in **Fig. 8c**. It also showed no apparent change is observed after the reaction. Based on the above results, it clearly suggests that the as-prepared PANI/FeUiO(1:5) nanohybrid has relatively high stability during the photocatalytic oxidation of alcohols.

3.4. Reaction mechanisms

To elucidate the possible reaction mechanism for the photocatalytic oxidation of benzyl alcohol over PANI/FeUiO-66 photocatalysts, a series of controlled experiments using different radical scavengers were carried out and the results were shown in **Fig. 9a**. Different radical scavengers were added to a system for removing the corresponding active species. That is, *p*-benzoquinone (BQ) for quenching superoxide radicals ($\bullet\text{O}_2^-$), AgNO_3 for quenching e^- , ethylenediamine tetraacetic acid dis-

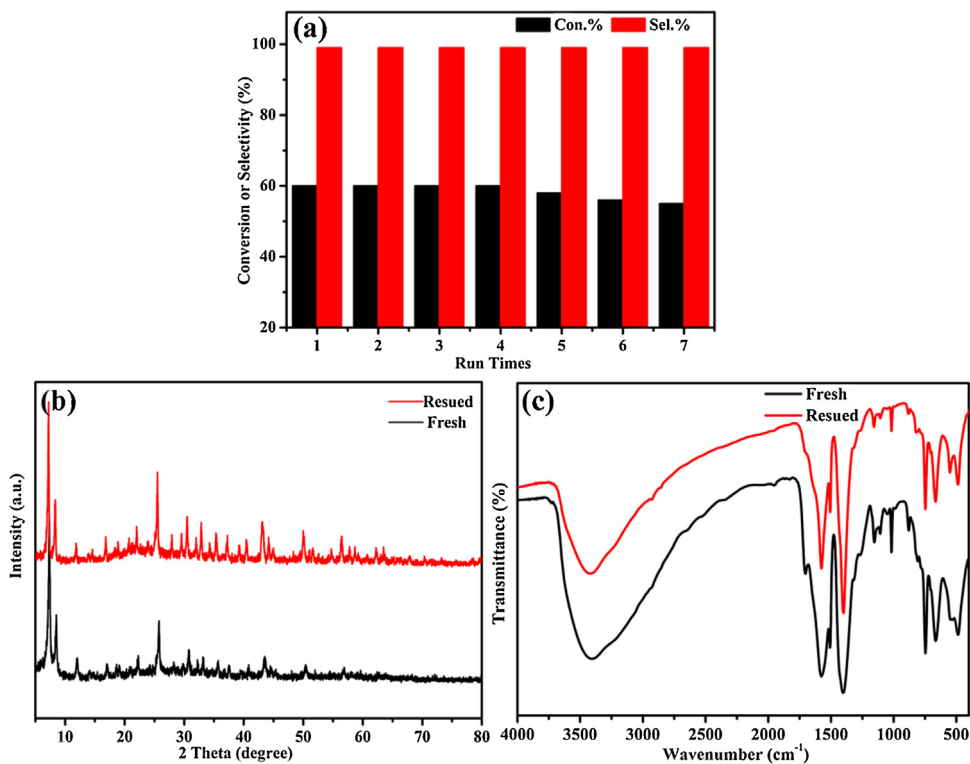


Fig. 8. The cycling runs at the oxidation of the benzyl alcohol over PANI/FeUiO(1:5) system (a);PXRD patterns (b) and FT-IR spectra (c) of PANI/FeUiO(1:5) before and after the catalytic reactions.

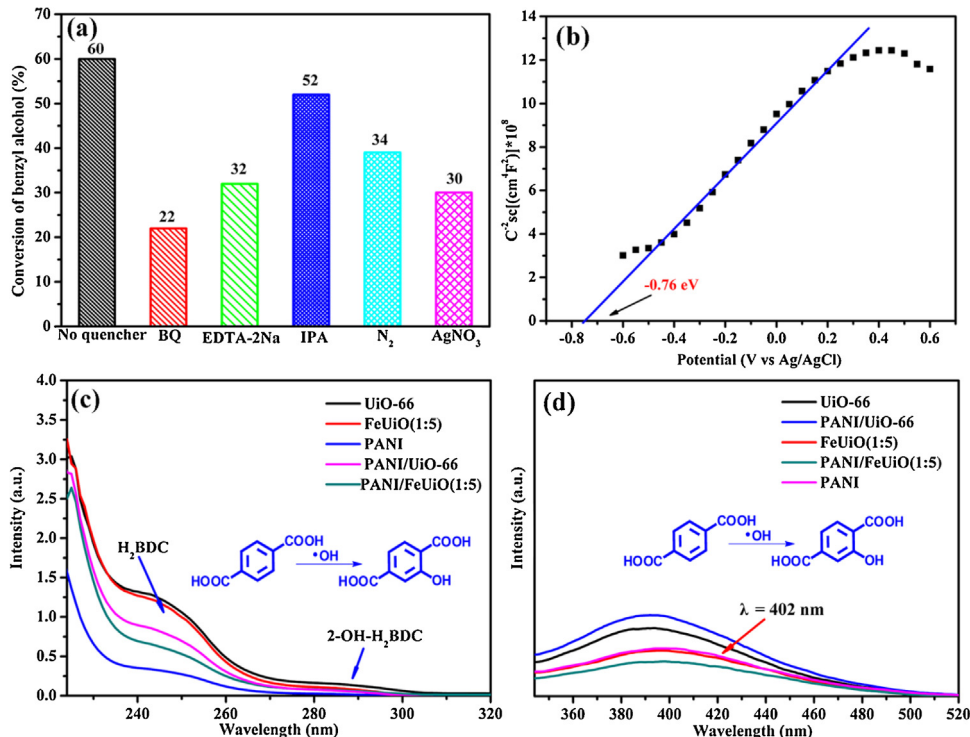


Fig. 9. Effects of different reactive species scavengers on the photocatalytic oxidation of benzylalcohol by PANI/FeUiO(1:5) (a) Mott-Schottky plot for the PANI/FeUiO(1:5) electrodes (b);UV/vis spectra (c) and fluorescence signal intensity (d) of different photocatalysts in H₂BDC solution in visible light irradiation.

odium (EDTA-2Na) for capturing holes (h^+), N_2 flow for excluding O_2 and isopropyl alcohol (IPA) for removing $\cdot\text{OH}$ [30,44,45]. When EDTA-2Na was added to the oxidation reaction systems, the conversion of BA decreased rapidly, indicating that photogenerated holes

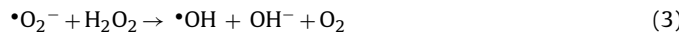
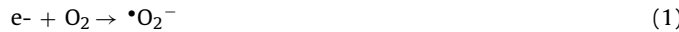
should be one of the main active species for the oxidation of benzyl alcohol. When the scavenger of BQ was added to the reaction system, the conversion of BA also decreased. Therefore, the $\cdot\text{O}_2^-$ also played an important role for the oxidation. To further confirm this

point, the reactions were carried out in the N_2 flow or with $AgNO_3$ added into the reaction system. It showed that the conversion of the BA was enormously decreased to 34% and 30%, respectively. The above results have synthetically demonstrated that the dissolved oxygen which could act as a photo-generated electron scavenger to produce $\bullet O_2^-$ radical species. Based on the above results, it is clear that the selective oxidation of BA to BAD is mainly triggered by the superoxide radicals and the positive holes.

While, when IPA was added to the reaction system, the photocatalytic activity decreased slightly, which suggests that $\bullet OH$ should not be an important contributor to the photocatalytic process. In order to confirm the presence of hydroxyl radicals, terephthalic acid (H₂BDC) was used as a probe molecule to detect $\bullet OH$ [30,46]. Fig. 9c and d displays the ultraviolet and fluorescence spectra of basic solution containing 1.0 mmol of H₂BDC in the presence of different photocatalyst after 1 h visible light irradiation, respectively. The weak ultraviolet and fluorescence peak were observed at 295 and 402 nm, which originated from 2-hydroxyterephthalic acid (2-OH-H₂BDC) generated by the reaction of H₂BDC with $\bullet OH$ under visible light irradiation, suggesting that a small amount of $\bullet OH$ was generated on the surface of UiO-66, FeUiO-66 and PANI/FeUiO-66.

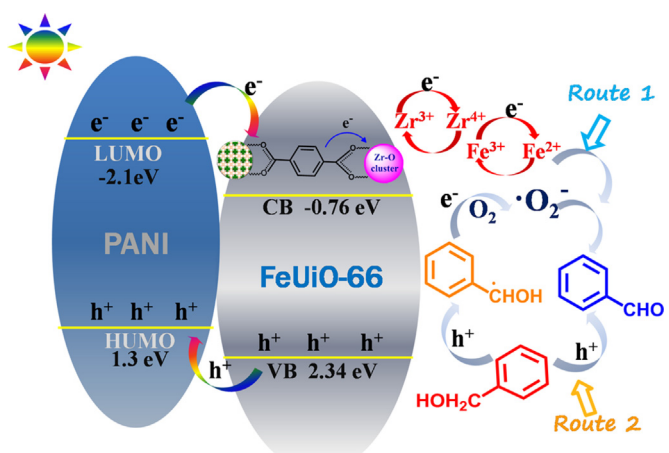
To understand the underlying mechanism for electrical conduction properties, the potential position of FeUiO(1:5) was measured by using Mott-Schottky plots (Fig. 9b). It shows an *n*-type semiconductor feature, as revealed by the positive slope of the plot. The flat band position is -0.76 V vs Ag/AgCl (-0.56 V vs NHE). The conduction band (CB) bottom of *n*-type semiconductor is 0.2 V above the flat band [47]. Therefore, the conduction band (CB) and the valence band (VB) of FeUiO-66 are -0.76 and 2.34 V, respectively. Besides, according to the literature, the LUMO and the HOMO potentials of PANI are -2.1 and 1.3 V, respectively [48]. The oxidation potential of $O_2/\bullet O_2^-$ is -0.33 V vs NHE, which is more negative than the CB of the FeUiO-66 and the LUMO of PANI, therefore, it was believed that both PANI and FeUiO-66 are capable of the generation of $\bullet O_2^-$ radicals by photoinduced electron reduction of molecular oxygen. As the previous studied, BA could be oxidized by h^+ directly when the value band potential of semiconductor is located in the range of $1.88 \sim 2.27$ V [49], so that the only FeUiO-66 is a candidate for the oxidation for the benzyl alcohol by h^+ directly. Considering the influence of the overpotential, benzaldehyde could not be further oxidized by the h^+ . These results are coincident with the above mentioned controlled experimental results. For the $\bullet OH$, it is clear that the HOMO position of PANI and FeUiO-66 valence band will not be appropriate for the direct generation of $\bullet OH$ radicals (2.4 V vs. NHE, pH=7). Besides the reaction system was performed in the water free system, $\bullet OH$ radicals could not be produced in this reaction process.

Therefore, the potential route for $\bullet OH$ radical generation in this PANI/FeUiO-66 photocatalytic system is the interaction of photoexcited electrons, $\bullet O_2^-$, and H_2O_2 [45].



Thus, the potential pathway for $\bullet OH$ generation in the PANI/FeUiO-66 photocatalytic system is the interaction of light-induced electron, $\bullet O_2^-$ and H_2O_2 .

On the basis of the above analysis, a possible mechanism for the oxidation of alcohol by PANI/FeUiO-66 composites under visible irradiation is proposed in Scheme 2. Firstly, PANI can be excited to generate electrons and holes under visible light irradiation. Photogenerated electrons and holes are generated on the HOMO



Scheme 2. The proposed mechanism for the photocatalytic process by PANI/FeUiO-66.

and LUMO of PANI when irradiated by visible light, respectively. Since the LUMO potential of PANI is more negative than the CB of FeUiO(1:5), the photo-generated electrons of PANI can be easily and directly transferred into the CB of FeUiO(1:5) through the well defined interface. According to the literature, the photocatalytic reduction of CO_2 over NH_2 -UiO-66 revealed that an electron transferred from the excited ligand to the Zr-O oxo-clusters (LMCT) to form Zr^{3+} under visible light then Zr^{3+} is responsible for CO_2 reduction to form $HCOO^-$ [50]. Similarly, the electron transferred from excited ligand to the Zr-O oxo-clusters (LMCT) to form Zr^{3+} under visible light and Zr^{3+} is oxidized to Zr^{4+} and then reacted with oxygen molecules to generate $\bullet O_2^-$ radicals. Moreover, when the Fe^{3+} are introduced into UiO-66, the synergistic effect of Fe and Zr species could responsible for the higher efficiency in charge separation, based on MMCT excitation [15]. Simultaneously, the excited holes produced by FeUiO-66 are injected into the HOMO of PANI. Furthermore, since the specific conjugated structure of PANI is an excellent material for transporting holes. As a result, the charge transfer efficiently inhibits the recombination of photo-generated electron-hole pairs, thereby enhancing the photocatalytic activity of PANI/FeUiO-66 photocatalyst. The holes on the surface of photocatalyst could induce the oxidation of alcohols to produce the corresponding cationic radicals, which will succulently react with $\bullet O_2^-$ to form the corresponding carbonyl compounds. Besides, the holes in the FeUiO-66 could oxidize the BA to BAD directly. From what has been discussed above, $\bullet O_2^-$ and h^+ are the main active species for the oxidation of alcohols. Moreover, virtue of unique advantage of the position of the CB and VB of FeUiO-66, alcohols could be selectively oxidized by the $\bullet O_2^-$ and h^+ to form the corresponding carbonyl compounds.

5. Conclusions

In summary, we have demonstrated a facile, reliable and cost-efficient method to prepare PANI/FeUiO-66 nanohybrids, which were used as eco-friendly photocatalysts for the oxidation of alcohols under visible-light irradiation. The superior photocatalytic efficiency of PANI/FeUiO-66 nanohybrids could be attributed two main aspects. On one hand, when Fe^{3+} doped into the framework of the UiO-66, it could broaden the visible light absorption region and enhance the separation efficiency of the photoproduced carriers. Moreover, by adjusting the content of Fe^{3+} , the photocatalytic activity is different. It was found that the FeUiO-66 composite with Fe: Zr molar ratio of 1: 5 shows the highest photocatalytic activity for the oxidation of alcohols. On the other hand, the energy band matching and excellent contacting between PANI and FeUiO-66 is assigned to

form heterostructures between them. It is in favor of the separation of photogenerated electron-hole pairs. The study on the photocatalytic mechanism of the PANI/FeUiO-66 nanohybrid implies that $\bullet\text{O}_2^-$ and h^+ should be the major contributors to the oxidation of alcohols. By virtue of unique advantage of the position of the CB and VB of FeUiO-66, alcohols could be selectively oxidized by the $\bullet\text{O}_2^-$ and h^+ . Last but not least, this study is a good example showing that MOFs-conductive conjugated polymers nanocomposites can be used as a class of efficient photocatalyst for the oxidation of alcohols with high selectivity at environmentally friendly conditions. It should open up the opportunities to the development of various MOFs based visible light photocatalysts for organic transformations in the future.

Acknowledgements

The research was financial supported by NSFC (21563026, 21163016), the Program for Changjiang Scholars and Innovative Research Team in University (IRT15R56), and the Innovation Team Basic Scientific Research Project of Gansu Province (1606RJIA324). We also thank the Key Laboratory of Eco-Environment-Related Polymer Materials (Northwest Normal University), Ministry of Education, for financial support.

References

- [1] X. Lang, X. Chen, J. Zhao, *Chem. Soc. Rev.* 43 (2014) 473–486.
- [2] J.C. Colmenares, R. Luque, *Chem. Soc. Rev.* 43 (2014) 765–778.
- [3] X. Jin, L. Ye, H. Wang, Y. Su, H. Xie, Z. Zhong, H. Zhang, *Appl. Catal. B: Environ.* 165 (2015) 668–675.
- [4] F.J. López-Tenllado, S. Murcia-López, D.M. Gómez, A. Marinas, J.M. Marinas, F.J. Urbano, J.A. Navío, M.C. Hidalgo, J.M. Gatica, *Appl. Catal.: Gen.* 505 (2015) 375–381.
- [5] R. Marotta, I. Di Somma, D. Spasiano, R. Andreozzi, V. Caprio, *J. Chem. Technol. Biotechnol.* 88 (2013) 864–872.
- [6] H. Liu, X. Dong, C. Duan, X. Su, Z. Zhu, *Ceram. Int.* 39 (2013) 8789–8795.
- [7] Y. Tian, B. Chang, J. Lu, J. Fu, F. Xi, X. Dong, *ACS Appl. Mater. Interfaces* 5 (2013) 7079–7085.
- [8] J. Xu, L. Luo, G. Xiao, Z. Zhang, H. Lin, X. Wang, J. Long, *ACS Catal.* 4 (2014) 3302–3306.
- [9] J. Tian, Z.Y. Xu, D.W. Zhang, H. Wang, S.H. Xie, D.W. Xu, Y.H. Ren, H. Wang, Y. Liu, Z.T. Li, *Nat. Commun.* 7 (2016) 11580.
- [10] X. Sun, Q. Yu, F. Zhang, J. Wei, P. Yang, *Catal. Sci. Technol.* 6 (2016) 3840–3844.
- [11] K. Manna, T. Zhang, M. Carboni, C.W. Abney, W. Lin, *J. Am. Chem. Soc.* 136 (2014) 13182–13185.
- [12] Z. Zhang, Y. Chen, X. Xu, J. Zhang, G. Xiang, W. He, X. Wang, *Angew. Chem. Int. Ed.* 53 (2014) 429–433.
- [13] F. Jeremias, V. Lozan, S.K. Henninger, C. Janiak, T. Dalton, (2013) 15967–15973.
- [14] Y. Yang, F. Wang, Q. Yang, Y. Hu, H. Yan, Y.Z. Chen, H. Liu, G. Zhang, J. Lu, H.L. Jiang, H. Xu, *ACS Appl. Mater. Interfaces* 6 (2014) 18163–18171.
- [15] Y. Fu, L. Sun, H. Yang, L. Xu, F. Zhang, W. Zhu, *Appl. Catal. B: Environ.* 187 (2016) 212–217.
- [16] T. Zhang, W. Lin, *Chem. Soc. Rev.* 43 (2014) 5982–5993.
- [17] J.L. Wang, C. Wang, W. Lin, *ACS Catal.* (2012) 2630–2640.
- [18] S. Wang, X. Wang, *Small* 11 (2015) 3097–3112.
- [19] N. Stock, S. Biswas, *Chem. Rev.* 112 (2011) 933–969.
- [20] D.T. Genna, A.G. Wong Foy, A.J. Matzger, M.S. Sanford, *J. Am. Chem. Soc.* 135 (2013) 10586–10589.
- [21] S. Kitagawa, *Chem. Soc. Rev.* 43 (2014) 5415–5418.
- [22] R. Shi, G. Liu, H. Liang, Y. Huang, Y. Tao, J. Zhang, *Inorg. Chem.* 55 (2016) 7777–7786.
- [23] M. Wen, Y. Kuwahara, K. Mori, D. Zhang, H. Li, H. Yamashita, *J. Mater. Chem. A* 3 (2015) 14134–14141.
- [24] D. Sun, W. Liu, M. Qiu, Y. Zhang, Z. Li, *Chem. Commun.* 51 (2015) 2056–2059.
- [25] R. Wang, L. Gu, J. Zhou, X. Liu, F. Teng, C. Li, Y. Shen, Y. Yuan, *Adv. Mater. Interfaces* 2 (2015).
- [26] Y. Chen, W. Huang, D. He, Y. Situ, H. Huang, *ACS Appl. Mater. Interfaces* 6 (2014) 14405–14414.
- [27] M. Radoičić, Z. Šaponjić, I.A. Janković, G. Čirić-Marjanović, S.P. Ahrenkiel, M.I. Čomor, *Appl. Catal. B: Environ.* 136–137 (2013) 133–139.
- [28] Q. Huang, S. Tian, D. Zeng, X. Wang, W. Song, Y. Li, W. Xiao, C. Xie, *ACS Catal.* 3 (2013) 1477–1485.
- [29] W. Wu, D. Pan, Y. Li, G. Zhao, L. Jing, S. Chen, *Electrochim. Acta* 152 (2015) 126–134.
- [30] Z. Sha, H.S. Chan, J. Wu, J. Hazard. Mater. 299 (2015) 132–140.
- [31] P. Xiong, Q. Chen, M. He, X. Sun, X. Wang, *J. Mater. Chem.* 22 (2012) 17485.
- [32] H. Wang, F. Yin, G. Li, B. Chen, Z. Wang, *Int. J. Hydrogen Energy* 39 (2014) 16179–16186.
- [33] L. Ge, C. Han, J. Liu, *J. Mater. Chem.* 22 (2012) 11843.
- [34] J. Mu, G. Ma, H. Peng, J. Li, K. Sun, Z. Lei, *J. Power Sources* 242 (2013) 797–802.
- [35] Y. Su, Z. Zhang, H. Liu, Y. Wang, *Appl. Catal. B: Environ.* 200 (2017) 448–457.
- [36] L. Yuan, C. Wan, X. Ye, F. Wu, *Electrochim. Acta* 213 (2016) 115–123.
- [37] R. Lin, L. Shen, Z. Ren, W. Wu, Y. Tan, H. Fu, J. Zhang, L. Wu, *Chem. Commun.* 50 (2014) 8533–8535.
- [38] K. Li, S. Gao, Q. Wang, H. Xu, Z. Wang, B. Huang, Y. Dai, J. Lu, *ACS Appl. Mater. Interfaces* 7 (2015) 9023–9030.
- [39] R. Jain, V. Luthra, S. Gokhale, *J. Magn. Magn. Mater.* 414 (2016) 111–115.
- [40] H. Li, Y. Zhao, Y. Wang, Y. Li, *Catal. Today* 259 (2016) 417–422.
- [41] L. Guo, F. Chen, X. Fan, W. Cai, J. Zhang, *Appl. Catal. B: Environ.* 96 (2010) 162–168.
- [42] X. Li, J. Liu, A.I. Rykov, H. Han, C. Jin, X. Liu, J. Wang, *Appl. Catal. B: Environ.* 179 (2015) 196–205.
- [43] H.R. Abid, H. Tian, H.M. Ang, M.O. Tade, C.E. Buckley, S. Wang, *J. Chem. Eng.* 187 (2012) 415–420.
- [44] J. Bi, Z. Zhou, M. Chen, S. Liang, Y. He, Z. Zhang, L. Wu, *Appl. Surf. Sci.* 349 (2015) 292–298.
- [45] L. Su, X. Ye, S. Meng, X. Fu, S. Chen, *Appl. Surf. Sci.* 384 (2016) 161–174.
- [46] M. Wen, Y. Kuwahara, K. Mori, D. Zhang, H. Li, H. Yamashita, *J. Mater. Chem. A* 3 (2015) 14134–14141.
- [47] Y.P. Yuan, L.S. Yin, S.W. Cao, G.S. Xu, C.H. Li, C. Xue, *Appl. Catal. B: Environ.* 168–169 (2015) 572–576.
- [48] L. Liu, L. Ding, Y. Liu, W. An, S. Lin, Y. Liang, W. Cui, *Appl. Catal. B: Environ.* 201 (2017) 92–104.
- [49] Z. Yang, X. Xu, X. Liang, C. Lei, Y. Wei, P. He, B. Lv, H. Ma, Z. Lei, *Appl. Catal. B: Environ.* 198 (2016) 112–123.
- [50] D. Sun, Y. Fu, W. Liu, L. Ye, D. Wang, L. Yang, X. Fu, Z. Li, *J. Chem. Eur.* 19 (2013) 14279–14285.